

Sidorenkite ($\text{Na}_3\text{MnPO}_4\text{CO}_3$): A New Intercalation Cathode Material for Na-Ion Batteries

Hailong Chen,[†] Qing Hao,[†] Olivera Zivkovic,[‡] Geoffroy Hautier,[†] Lin-Shu Du,[‡] Yuanzhi Tang,[§] Yan-Yan Hu,^{‡,||} Xiaohua Ma,[†] Clare P. Grey,^{‡,||} and Gerbrand Ceder*,^{†,†}

[†]Department of Materials Science and Engineering, Massachusetts Institute of Technology, 77 Massachusetts Ave, Cambridge, Massachusetts 02139, United States

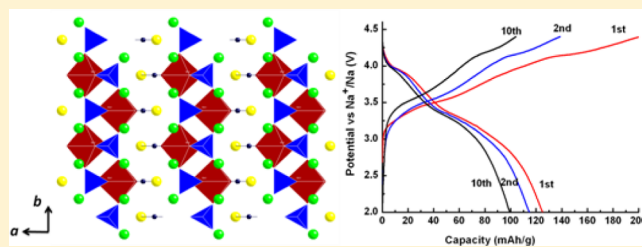
[‡]Department of Chemistry, Stony Brook University, 100 Nichols Road, Stony Brook, New York 11794-3400, United States

[§]School of Earth and Atmospheric Sciences, Georgia Institute of Technology, 311 Ferst Dr., Atlanta, Georgia 30332-0340, United States

^{||}Department of Chemistry, Cambridge University, Lensfield Rd, CB2 1EW, Cambridge, United Kingdom

Supporting Information

ABSTRACT: Na-ion batteries represent an effective energy storage technology with slightly lower energy and power densities but potentially lower material costs than Li-ion batteries. Here, we report a new polyanionic intercalation cathode material of an unusual chemical class: sidorenkite ($\text{Na}_3\text{MnPO}_4\text{CO}_3$). This carbonophosphate compound shows a high discharge capacity (~125 mAh/g) and specific energy (374 Wh/kg). *In situ* X-ray diffraction measurement suggests that sidorenkite undergoes a solid solution type reversible topotactic structural evolution upon electrochemical cycling. *Ex situ* solid state NMR investigation reveals that more than one Na per formula unit can be deintercalated from the structure, indicating a rarely observed two-electron intercalation reaction in which both $\text{Mn}^{2+}/\text{Mn}^{3+}$ and $\text{Mn}^{3+}/\text{Mn}^{4+}$ redox couples are electrochemically active.



KEYWORDS: Na-ion batteries, batteries, intercalation, cathode, carbonophosphates, phosphocarbonates, ^{23}Na NMR, MAS NMR, hydrothermal

1. INTRODUCTION

The rapidly growing global consumption of energy calls for new energy conversion and storage techniques with increased high energy density and efficiency. Li-ion batteries (LIBs) have been extensively studied during the past three decades as they can provide higher voltage (3–4 V) and specific energy (~100–180 Wh/kg) than other rechargeable batteries, such as lead-acid and Ni–Cd batteries. Na-ion batteries (NIBs) represent another promising rechargeable battery technology.^{1–3} The operating mechanisms of NIBs and LIBs are similar, with Na ions shuttling between electrodes instead of Li ions. Compared to LIBs, NIBs are expected to have a slightly lower voltage.^{1,2} However, due to the much higher abundance of Na than Li in the earth's crust, it is possible that NIBs can be made at lower cost than LIBs in the future, which is much desired for large-scale energy storage. Furthermore, aluminum foils can be used as the current collectors for anodes in NIBs, because sodium does not alloy with aluminum;^{4,5} while in LIBs more expensive copper foils are used as the current collectors for anodes because aluminum alloys with lithium. This aspect represents another potential advantage of NIBs in large-scale energy storage.

Recently, a number of layered oxides have been investigated for their properties as cathode materials for NIBs, such as P2–

Na_xCoO_2 ,⁶ Na_xMnO_2 ,^{7,8} $\text{Na}_x(\text{Ni}_{1/2}\text{Mn}_{1/2})\text{O}_2$,⁹ and P2– $\text{Na}_x(\text{Fe}_{1/2}\text{Mn}_{1/2})\text{O}_2$.³ These oxides have high theoretical capacity (up to ~250 mAh/g) with a one-electron redox reaction, where the valence of the transition metal varies between +3 and +4. However, the high theoretical capacities have yet to be fully achieved experimentally. Many of these layered oxides show complicated phase transitions during electrochemical cycling, which may be caused by Na-vacancy ordering and/or layer shearing/sliding.⁶ It is not clear yet to what extent these phase transformations may limit practical capacity or cycle life. Some layered oxides, such as $\text{Na}-(\text{NiFeMn})_{1/3}\text{O}_2$,¹⁰ and $\text{Na}_{0.85}\text{Li}_{0.17}\text{Ni}_{0.21}\text{Mn}_{0.64}\text{O}_2$,¹¹ show solid solution-like behavior during cycling, though only ~50% of their theoretical capacity can be achieved. Polyanion-type cathode materials for NIBs have also been studied, including $\text{Na}_3\text{Fe}_3(\text{PO}_4)_4$,¹² $\text{NaMnFe}_2(\text{PO}_4)_3$,¹³ NaFePO_4 ,^{14–16} and $\text{Na}-\text{FeSO}_4\text{F}$.¹⁷ Here, we report a new promising polyanionic carbonophosphate cathode material for NIBs, sidorenkite ($\text{Na}_3\text{MnPO}_4\text{CO}_3$).

Received: March 11, 2013

Revised: June 11, 2013

Published: July 11, 2013

Carbonophosphates are a rarely explored chemical class and were previously reported to only occur in rare natural minerals, such as sidorenkite¹⁸ and bonshtedtite ($\text{Na}_3\text{FePO}_4\text{CO}_3$). The structure of the reported sidorenkite mineral¹⁹ is shown in Figure 1. MnO_6 octahedra are connected by PO_4 tetrahedra to

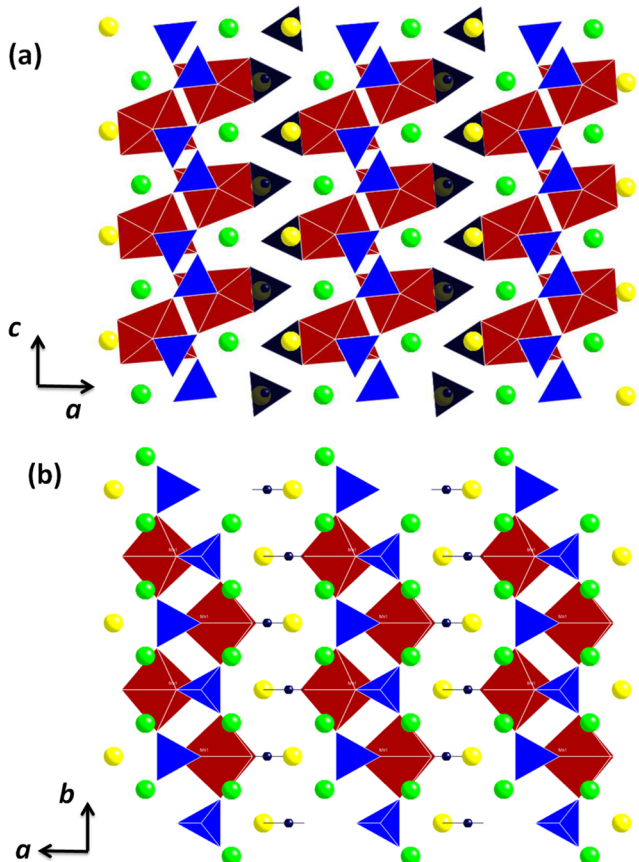


Figure 1. The structure of $\text{Na}_3\text{MnPO}_4\text{CO}_3$ viewed along [010] (a) and [001] (b). Mn octahedra, brown; PO_4 tetrahedra, blue; CO_3 triangular planar, black; sodium, green (Na1 site) and yellow (Na2 site) spheres.

form double layers. The CO_3 groups share an oxygen edge with MnO_6 octahedra and point toward a “2D slab” space that accommodates the Na atoms. Na atoms are located in two different interstitial sites: The Na(1) site (green in Figure 1) coordinates with seven O atoms, while the Na(2) site (yellow in Figure 1) coordinates with six O atoms. The multiplicities of Na(1) and Na(2) are 4 and 2, respectively; i.e., there are two Na(1) sites and one Na(2) site per formula unit, and the average Na–O bond distance is 2.50 Å, which is slightly larger than that in NaMnO_2 (2.36 Å). Previous computations have suggested that the sidorenkite structure may have good intercalation characteristics.²⁰ To explore this, lithium iron and manganese carbonophosphates were recently synthesized and tested as Li-ion battery cathodes.²¹ Here, we report that in a Na-ion battery, $\text{Na}_3\text{MnPO}_4\text{CO}_3$ shows a high discharge capacity of ~125 mAh/g, which is 66% of its theoretical capacity (191 mAh/g).

To study the Na deintercalation process in $\text{Na}_3\text{MnPO}_4\text{CO}_3$, a solid-state nuclear magnetic resonance (NMR) investigation on electrochemically charged/discharged materials is performed. ^6Li and ^{7}Li Magic Angle Spinning NMR (MAS NMR) spectroscopy has been extensively used to study a wide

variety of paramagnetic positive electrode materials for LIBs due to its high sensitivity to short-range ordering, oxidation state, coordination number, and local symmetry.^{22–27} NMR studies have been performed with the quadrupolar ($I = 3/2$) nucleus ^{23}Na to study various sodium salts^{28–33} including a few electrode materials such as Na_xCoO_2 ,³⁴ $\text{Na}_{2/3}\text{Co}_{2/3}\text{Mn}_{1/3}\text{O}_2$,³⁵ and $\text{Na}_3\text{Fe}_3(\text{PO}_4)_4$.¹² ^{23}Na solid-state NMR is applied here to identify Na^+ ion sites in the pristine material, to follow the Na occupancy change upon charge and discharge, and to determine the reversibility of the intercalation/deintercalation process in sidorenkite. The results indicate that both $\text{Mn}^{2+}/\text{Mn}^{3+}$ and $\text{Mn}^{3+}/\text{Mn}^{4+}$ redox couples are active and more than one (~1.3) Na per formula unit can be reversibly intercalated/deintercalated, making this compound one of a few reported manganates where two-electron reactions can occur.

2. METHODS

2.1. Synthesis. A typical synthesis of $\text{Na}_3\text{MnPO}_4\text{CO}_3$ is as follows: Separately, 0.02 mol of $\text{Mn}(\text{NO}_3)_2 \cdot 4\text{H}_2\text{O}$ was dissolved in 50 mL of water to form a clear solution (A). A total of 0.02 mol of $(\text{NH}_4)_2\text{HPO}_4$ and 20 g of Na_2CO_3 were dissolved in 100 mL of water to form a clear solution (B). Solution A was then quickly added to solution B under fast magnetic stirring. The obtained slurry was then transferred to a glass bottle sealed with a cap. The bottle was heated in a 120 °C oil bath in an Ar flushed glovebox for 4–72 h, after which it was taken out of the oil bath and slowly cooled down to room temperature. The slurry was centrifuged and washed with distilled water and methanol several times to separate the solids. The solid samples were dried in a vacuum oven at 40 °C overnight.

2.2. Electrochemical Tests. For electrochemical characterization, the as-prepared sample was first mixed with carbon (super P; 8S:15 wt %) followed by ball milling at 500 rpm for 4–6 h. The milled powder was then mixed again with more carbon and PTFE binder to reach an overall composition of active material:carbon:PTFE = 60:30:10 (wt %). A high carbon content was used to minimize any rate limiting factors from the electrode design. The mixture was ground and roll-pressed into self-standing cathode films. Coin cells (CR2016) were assembled in an Ar-filled glovebox. Each cell typically contains 4–8 mg of active material, separated from a Na metal foil anode by a piece of Celgard 2325 separator (Celgard, Inc., USA) and a piece of glass fiber separator (VWR). A 1 M solution of NaPF_6 (Sigma-Aldrich, 98%) in ethylene carbonate/dimethyl carbonate (1:1) was prepared as the electrolyte. Electrochemical experiments were carried out on a battery cycler (Arbin Instruments, College Station, TX) in galvanostatic mode at various rates.

2.3. XRD and SEM Characterizations. All the powder samples were characterized by X-ray powder diffraction (XRD) using a Rigaku miniflex II diffractometer ($\text{Cr } K\alpha$, $\lambda = 2.2897$ Å). *Ex situ* and *in situ* XRD of some powder samples were also collected using synchrotron radiation sources at beamlines X16C ($\lambda = 0.699$ Å) and X14A ($\lambda = 0.774$ Å) at the National Synchrotron Light Source at Brookhaven National Laboratory (NSLS-BNL). Refinements of the XRD patterns were performed using the GSAS code. Scanning electron microscope (SEM) images were taken using a JEOL 6032 SEM.

2.4. Solid-State Nuclear Magnetic Resonance (NMR) Measurements. ^{23}Na MAS NMR experiments were performed at 52.8 MHz on a CMX-200 spectrometer in a 4.7 T magnetic field using a 1.8 mm MAS probe with spinning speeds (ν_r) of 35 and 38 kHz. Additional experiments were performed at 79.2 and 132.2 MHz in a 7.05 and 11.75 T field, respectively, using a 1.3 mm MAS probe with 35–50 kHz spinning speeds. Both probes were designed and manufactured by Dr. Ago Samoson and co-workers (NICFB, Tallinn, Estonia). A rotor synchronized spin-echo pulse sequence ($90^\circ - \tau - 180^\circ - \tau_1$ -acquisition) was used with a 90° pulse length of 1 μs . The pulse delay was 0.1 s. Additional ^{23}Na spectra were acquired with the projection-MATPASS sequence at the ^{23}Na frequency of 132.2 MHz at a field strength of 11.75 T and at a spinning speed of 50 kHz. Further details concerning the projection-MATPASS experiment can

be found in the Supporting Information. ^{23}Na MAS NMR spectra were deconvoluted and modeled using the mat3NMR program written by Dr. J. van Beek.³⁶ Data acquired using the projection-MATPASS sequence were processed with GSIM software, version 0.20.1.³⁷

2.5. Ex Situ X-Ray Absorption Spectroscopy Measurements.

X-ray absorption near edge structure (XANES) spectroscopy data were collected on a series of charged and discharged samples at beamline X18B at NSLS-BNL. To prepare the samples in charged states, the cells were electrochemically charged to different capacities, then stopped and taken apart. The cathode films were separated from the disassembled cells and washed with DMC. The discharged samples were prepared by first charging the cell to 4.5 V then discharging to different voltages, such as 3.7, 3.3, 2.5, and 2 V. Three reference compounds (MnO , Mn_2O_3 , and MnO_2) were used as standards for the oxidation state. A monochromator consisting of a pair of Si (111) crystals was used, with one crystal detuned by 40% to avoid high order harmonics. A Mn foil (6539 eV) was used for energy calibration. Data analysis was performed using the Ifeffit software.³⁸ The edge position, defined as the first inflection point of the main edge, was used to estimate the oxidation state of the samples.

2.6. Ab Initio Computations. Computations were performed within the density functional theory (DFT) framework, with the Vienna ab initio software package (VASP),³⁹ within the generalized gradient approximation by Perdew–Burke–Ernzerhof (GGA-PBE)⁴⁰ and projector augmented wave pseudopotentials (PAW).⁴¹ A Hubbard U of 3.9 eV was used to correct for the self-interaction errors on the d electrons of Mn.⁴² This U value was obtained by fitting binary oxide reaction energies following the methodology of Wang et al.⁴³ The computations' detailed parameters are available in Jain et al.⁴⁴

Voltages were computed following Aydinol et al. and neglecting entropic contributions.⁴⁵ When several orderings of Na ions and vacancies were possible for the desodiated structures, we computed with DFT the 10 orderings with lowest electrostatic energy from a large set of candidate arrangements enumerated with an algorithm similar to the one developed by Hart and Forcade.⁴⁶

3. RESULTS

3.1. Synthesis. Sideronkite samples were prepared by hydrothermal methods. Figure 2 shows the high-resolution

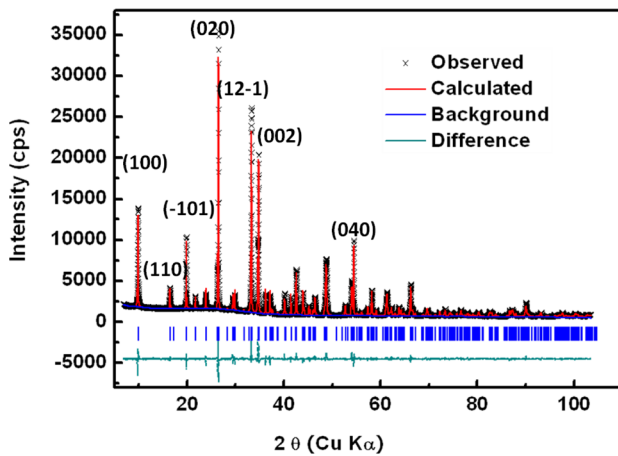


Figure 2. The XRD pattern of synthetic sidorenkite and Rietveld refinement using space group $P2_1/m$. $R_{wp} = 0.065$, $R_p = 0.047$, $\chi^2 = 5.75$.

powder XRD pattern of the sample synthesized at 120 °C for 3 days. Rietveld refinement confirms that the synthetic sidorenkite has the same structure as the mineral, but with slightly different lattice parameters, likely due to impurities present in the natural mineral samples (see Table S1 in the Supporting Information for detailed refinement results).

Sidorenkite can form over a rather wide temperature range from 90 to 240 °C in the hydrothermal synthesis, if the reaction time is properly adjusted. Figure 3a shows the SEM image of

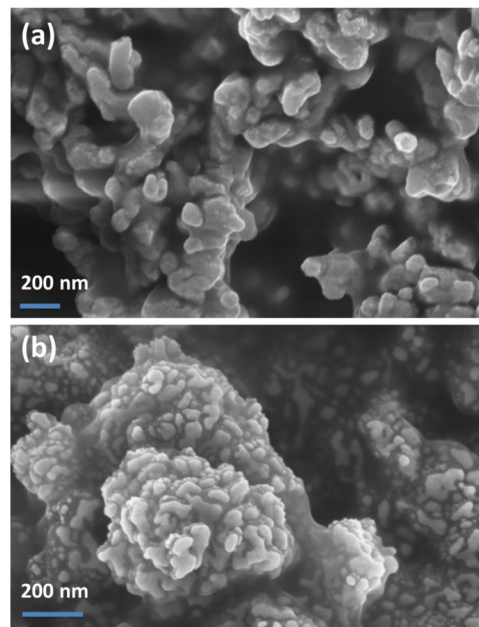


Figure 3. SEM images of $\text{Na}_3\text{MnPO}_4\text{CO}_3$ (a) as-synthesized and (b) after ball-milling.

sidorenkite synthesized at 120 °C, 72 h. The particles are agglomerated and plate-like with a length and width of ~200 nm and a thickness of ~100 nm. The particle size can be controlled by varying the time and temperature of the hydrothermal reaction or by using high energy ball-milling. In this work, we used both approaches to control the particle size.

Figure 3b shows the SEM image of the sidorenkite sample synthesized at 120 °C, 72 h and followed by ball-milling at 500 rpm for 6 h with carbon. The ratio of sidorenkite to carbon is 85:15 wt %. The particle size is reduced to ~50–100 nm after ball milling, but the agglomeration of the particles becomes more significant than in the pristine sample. The morphology of the particles also becomes more irregular after milling.

3.2. Electrochemical Tests. The sidorenkite sample synthesized at 120 °C, 72 h and ball-milled at 500 rpm for 6 h was electrochemically tested in coin cells. Figure 4a shows selected charge and discharge curves of sidorenkite between 2 and 4.4 V at a C/100 rate in the first, second, and 10th cycles. The first charge capacity is ~200 mAh/g, which is slightly larger than the two-electron theoretical capacity (191 mAh/g). This is probably due to some parasitic reactions, such as the decomposition of the electrolyte, especially at high voltage. The first discharge capacity is ~125 mAh/g, which is ~66% of the theoretical capacity and corresponds to the insertion of 1.3 Na per formula unit. This clearly indicates that the $\text{Mn}^{3+}/\text{Mn}^{4+}$ redox couple is, at least partially, active. The reversible capacity gradually decreases in the following cycles and stabilizes at around 100 mAh/g after 10 cycles, as shown in Figure 4d. The coulombic efficiency is low for the first cycle but improves in subsequent cycles. The rate performance of sidorenkite was also tested. Discharge curves of sidorenkite at various rates in the first cycle are shown in Figure 4c. No significant capacity drop was observed when the rate increased from C/100 to C/30. At a moderate rate of C/5, the discharge capacity is ~100

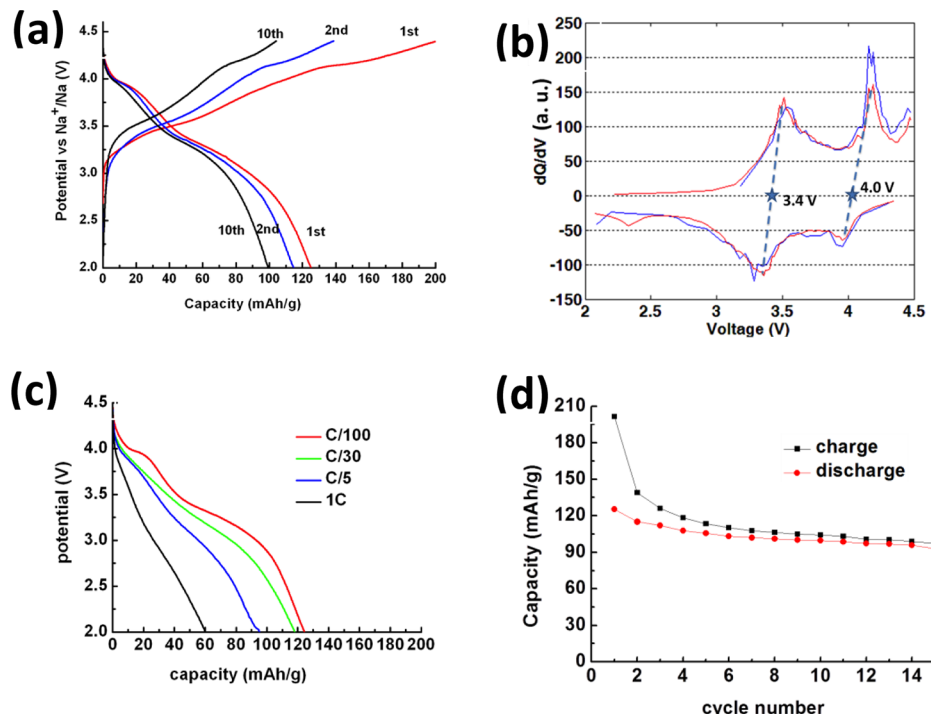


Figure 4. (a) The voltage curves of sidorenkite at the first, second, and 10th cycles with a C/100 rate. (b) dQ/dV plot of the first (red line) and second (blue line) cycles. The asterisks indicate the average of each peak on charging and discharging. (c) The discharge curve of sidorenkite at different rates. (d) The capacity retention of sidorenkite at C/100 rate.

mAh/g. When the rate increases to 1C, the capacity drops to ~60 mAh/g. More optimization will certainly be necessary to improve the rate performance, but even without extensive optimizations, sidorenkite still shows a promising rate performance.

Two obvious plateaus are observed in both the charge and discharge curves, plausibly corresponding to Mn^{2+}/Mn^{3+} and Mn^{3+}/Mn^{4+} redox reactions, respectively. To demonstrate these two redox steps better, a dQ/dV plot extracted from the cycling data is shown in Figure 4b. Two cathodic and two anodic peaks are observed in both the first and second cycles. The cathodic peaks are at 3.5 and 4.15 V, while the anodic peaks are at 3.3 and 3.95 V. The equilibrium voltages of the two reactions can be estimated by taking the average of the cathodic and anodic peaks, yielding values of 3.4 and 4.0 V, as shown in the figure. This result is in good agreement with the voltages computed through *ab initio* computations using the same method reported in our previous work,²⁰ which indicated that the average Mn^{2+}/Mn^{3+} redox potential should be about 3.1 V and the average Mn^{3+}/Mn^{4+} redox potential should be around 4.0 V. The predicted voltage for Mn^{2+}/Mn^{3+} is ~0.3 V lower than the experimental result. We cannot account for this discrepancy at this time. It is toward the high side of the errors one would expect for DFT+U^{47,48} though it is possible that "U" is not well calibrated for this structure or the structural changes upon Na extraction are not properly represented in the calculations. Finally, it is worth noting that the experimental capacity that appears as a gradually rising potential above 4.2 V on charge, indicates that electrolyte decomposition becomes pronounced at this voltage, giving rise to the "extra" capacity seen on charging.

3.3. In Situ XRD. *In situ* XRD experiments were performed using synchrotron X-ray sources. A schematic of the *in situ* cell is shown in Figure S1 of the Supporting Information. The

charge and discharge capacities obtained with the *in situ* cell are lower than those obtained in the laboratory with *ex situ* coin cells, with charge capacity being ~160 mAh/g and discharge capacity being ~70 mAh/g. Several factors likely contribute to this lower capacity. To limit the beam time needed, the cell was cycled at a higher rate of C/20. In addition, the *in situ* cell may not be as well sealed as our coin cells, and the metallic Na anode is very sensitive to air and moisture, which may lead to anode polarization. The compression on this cell (i.e., the pressure on the two current collectors) is also poor. Figure 5 shows the XRD patterns of the cell assembly collected in the first cycle, around the (100), (−121), and (002) reflections of sidorenkite (see Figure S2 in the Supporting Information for the full patterns). Due to the smaller particle size of the ball-

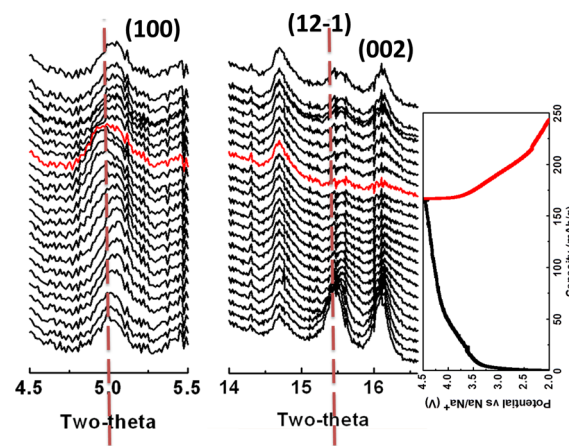


Figure 5. *In situ* XRD patterns of sidorenkite around 5° and 15° two-theta. Discharge starts from the red pattern. The wavelength used is 0.6994 Å.

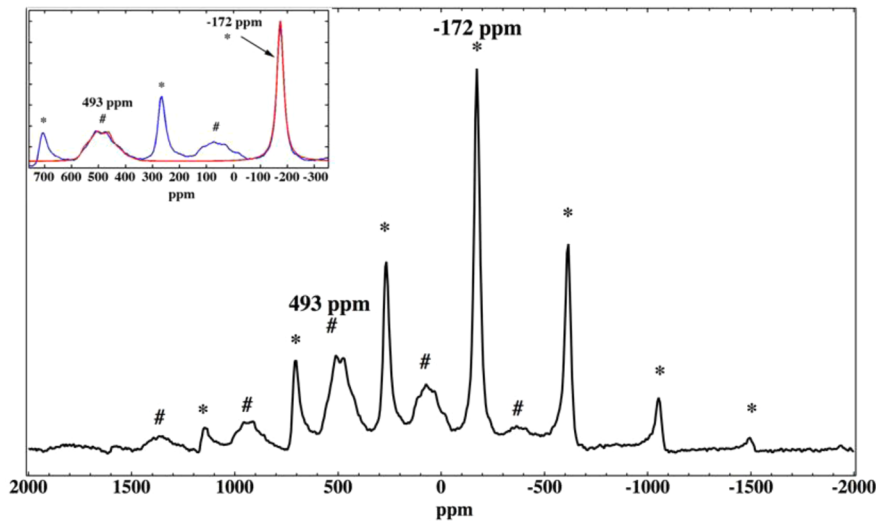


Figure 6. ^{23}Na MAS NMR spectrum of pristine sidorenkite acquired on a 7.05 T magnet at a 35 kHz spinning speed. The inset shows the experiment (blue line) and simulation of the isotropic resonances at -172 and 493 ppm. Spinning side bands are marked with * and #. Parameters used in the simulations are, for the -180 ppm site, $C_Q = 1.2$ MHz, $\eta = 0.0$, $\delta_{\text{iso}} = -168$ ppm; for site at ~ 500 ppm, $C_Q = 4.4 \pm 0.2$ MHz, $\eta = 0.5 \pm 0.1$, $\delta_{\text{iso}} = 569 \pm 8$ ppm.

milled sample and the presence of noncrystalline materials in the cell (liquid electrolyte, carbon black, and glass fiber separator, etc.), the diffraction peaks from sidorenkite are much broader and weaker than those from the pristine powder sample (Figure 2). During charging, the (100) peak first shifts to higher two-theta values and then shifts back, which indicates that the change of cell parameter a is not monotonic upon Na extraction. The (-121) and (002) reflections shift to higher two-theta values and lose intensity, likely indicating shrinking of the unit cell along the b and c axes. The peak shifts on discharging indicate a partially reversible process; the peak positions and intensities do not completely revert back to the pristine state, which is consistent with the large irreversible capacity obtained from the *in situ* cell. In the cycling range observed, no pronounced new reflections are seen, implying that sidorenkite adopts a solid solution-like pathway upon Na extraction and insertion. The *in situ* XRD patterns of another cell, where a sample with large particle size was used to increase the intensity of the XRD peaks, are shown in the Supporting Information (Figure S3). Due to the large particle size, the discharge capacity is low. However, the shifting of the peaks during the charging process is more clearly demonstrated, being consistent with that observed in the first *in situ* cell.

3.4. NMR Spectroscopy. To understand the Na insertion/extraction mechanism further, *ex situ* solid state NMR experiments were performed on samples that are charged/discharged to different capacities/voltages. The ^{23}Na MAS NMR spectrum of pristine sidorenkite obtained at 7 T contains two isotropic resonances (Figure 6), a relatively narrow peak at around -172 ppm, and a broad peak centered at 493 ppm, consistent with the two crystallographic sites in the structure. The broadening of the two resonances is attributed to the second-order quadrupolar interaction, which is not completely removed by MAS. The difference in the peak width of the two resonances indicates that one Na site is in a much more disordered (asymmetric) environment than the other. A simulation of this broad resonance at around 493 ppm (Figure 6 inset) yielded the following NMR parameters: isotropic chemical shift, $\delta_{\text{iso}} = 569$ ppm, quadrupole coupling constant, C_Q 4.4 MHz, and asymmetry parameter, η , 0.5. Note that the

significant shift of the resonance from its isotropic chemical shift value (569 ppm) is a consequence of the second-order part of the quadrupolar interaction, the shift depending strongly on the field strength. The line broadening of the site centered at -172 ppm is too small to allow an accurate estimate of the quadrupolar parameters, but based on the simulations, the C_Q is no more than approximately 1.3 MHz. Considering the local environments of the sodium sites, Na(1) is located in pentagonal bipyramidal coordination of O^{2-} anions (Figure 7a), while Na(2) is located in distorted hexagonal O^{2-} coordination (Figure 7b). We therefore assign the more symmetric Na(1) environment to the resonance at -172 ppm on the basis of its smaller C_Q value, while the 493 ppm resonance is assigned to Na(2). An integrated ratio of 1.5:1 for the intensities of Na(1)/Na(2) was obtained, which is less than expected from the multiplicity ratio of 2:1. However, we have not taken into account any errors that may arise from the nonquantitative excitation of the broad sideband manifolds caused by the paramagnetic interactions and sites with very different quadrupolar parameters,⁴⁹ particularly when spin-echo sequences with π pulses are used. High field experiments (performed with a projection-MATPASS sequence (see Supporting Information Figure S4)) yielded a similar intensity ratio.

Spectra were obtained of electrodes that were charged to specific states of charge as shown in Figure 8a. A summary of the shifts obtained at various stages of charge (and discharge) with proposed stoichiometries are given in Table S2 (in the Supporting Information) along with quantitative estimates of site occupancy based on the peak areas.

Note that the spectra were acquired at lower fields (4.7 T) than the spectrum shown in Figure 6. Broader line widths are therefore expected as well as larger quadrupolar induced shifts, the latter resulting in slight differences in the peak maxima as compared to those seen in Figure 6. The ^{23}Na spectrum of a sample extracted from a cell charged to 3.5 V (i.e., following the removal of 0.5 Na^+ ions per formula unit) shows two distinct signals at -180 ppm and -13 ppm. The peak at -180 ppm corresponds to the Na(1) site found in pristine material nearby predominantly Mn^{2+} ; the new resonance seen at -13 ppm is

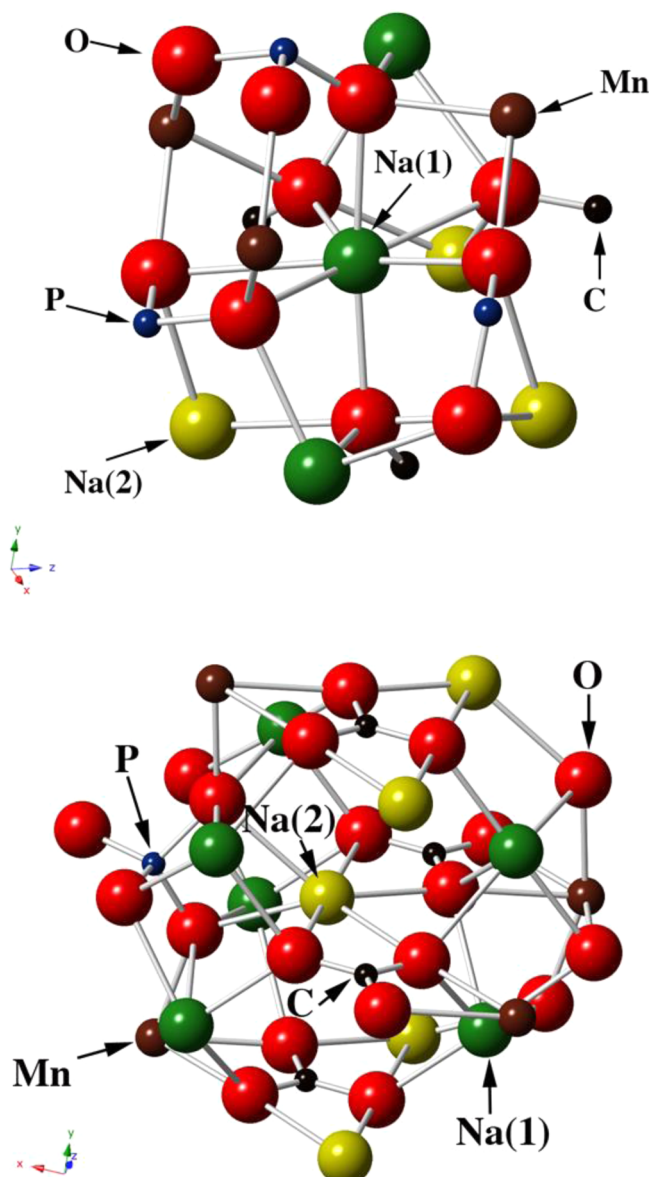


Figure 7. (a) The local environment of the Na(1) site in the sidorenkite structure. Na⁺ coordination to seven oxygen ions gives rise to six Na⁺–O–Mnⁿ⁺ interactions; Na⁺–O–Mnⁿ⁺ angles are 114.8°, 83.2°, 88.1°, 78.2°, 88°, and 82.8°. (b) The Na(2) local environment. Na⁺ ion coordination to six oxygen ions gives rise to four Na⁺–O–Mnⁿ⁺ interactions/ Two Na⁺–O–Mnⁿ⁺ angles are 130°, and the rest are 165.9° and 176.2°.

assigned to the Na(1) ions in an environment containing either a mixed Mn^{2+/3+} or an all Mn³⁺ environment. It is nontrivial to rationalize the Fermi-contact shifts in terms of the specific bonding arrangements in highly distorted structures, and often ab initio calculations are required.⁵⁰ But, we note that an increase of oxidation state often (but not always) correlates with an increase in shift due to an increase in covalence.^{51–54} The 570 ppm resonance assigned to Na(2) is not observed, suggesting that Na⁺⁽²⁾ ions are preferentially extracted from the lattice over Na(1) ions. The signal from the remaining Na(2) ions is most likely obscured by the much larger spinning sidebands of the Na(1) peak (~ 570–750 ppm region). Compared with the pristine material, the area of the –180 ppm Na(1) peak in material charged to 3.5 V has dropped by ~50%

(Table S1), indicating that 50% of Na(1) remains in a Mn²⁺ environment, while the rest is in a Mn³⁺ or mixed Mn^{2+/3+} environment centered at –13 ppm.

On further charging to 3.83 V (i.e., on extraction of approximately one Na⁺ ion), most noteworthy is the observation of a broad shoulder to higher frequencies of the resonance at –13 ppm that spreads over a few hundred ppm, which we assign to Na⁺ cations nearby Mn³⁺. The Na(2) ions are again not observed in this NMR spectrum. The area of the –180 ppm peak dropped to approximately 13% of the area of this peak in the pristine material, indicating that only a small amount of the Mn²⁺ environment remains. Since in theory, the material should only contain Mn³⁺ ions, the residual Mn²⁺ is most likely associated with heterogeneities in the electrode and the difficulty in activating the whole electrode material: oxidation of Mn³⁺ to Mn⁴⁺ has already commenced before some of the residual electrode is activated. An intense and broad peak at 92 ppm can be observed in the material charged to 4.09 V with weaker peaks at –180 and –13 ppm. The area of the –180 ppm peak is only 2.15% of that of the pristine material while the total intensity of the 4.09 V spectrum has dropped to 45%, as compared to the pristine material, consistent with an observed capacity of 142 mAhg⁻¹ and the extraction of 1.3 Na⁺ ions per formula unit. On charging to 4.5 V (and the extraction of two Na⁺ ions per formula unit), a very broad resonance centered at 194 ppm dominates the spectrum (Figure 8a, inset a), which is ascribed to Na(1) surrounded by Mn⁴⁺, and accounts for 46% of the total intensity as compared with the Na(1) site intensity of the pristine material. This is consistent with the extraction of half the Na(1) ions and all of the Na(2) ions. To illustrate the extraction sequence of Na ions and the change in the local environments of the residual Na ions during the charging process, as determined from the NMR spectra in Figure 8a, a schematic cartoon is drawn in Figure 8b. The Na ions at the Na(2) site are extracted first, and then 1/2 of the Na ions on the Na(1) site are extracted, which accounts for the 2-e theoretical capacity.

The resonance at –13.9 ppm due to the mixed Mn^{2+/Mn³⁺ environment is observed again on discharging to 3.7 V (corresponding to a capacity of 31 mAh/g; Figure 9) and neither resonance due to either Na(1) or Na(2) nearby Mn²⁺ are seen. On further discharging to 3.3 V (in the middle of the second lower voltage process based on the potential; discharge capacity 62 mAh/g; 0.6 Na⁺ intercalated), the Na(1) site at –180 ppm appears but the Na(2) site at approximately 500 ppm is not clearly observed at the low fields used to acquire these spectra. Use of higher fields (11.8 T) and fast spinning does, however, allow this resonance to be observed (Figure S4). The intensity ratio of Na(2) (540 ppm) and Na(1) (–13.9 and –180 ppm) sites is 1:8 and is consistent with the reinsertion of ions into the Na(2) site during the second process. The Na(2) sites are clearly observed in the ²³Na MAS NMR spectrum of the material discharged to 2 V after charging to 4.5 V (Figure 9; enlarged spectrum, Figure S6). The relative intensity of the –180 ppm Na(1), Mn²⁺ resonance, in comparison to the –13.9 ppm site, has also increased noticeably. The capacity on discharge was only 125 mAh/g, or 66% of the theoretical capacity, indicating intercalation of only 1.3 Na⁺ ions in the structure, consistent with the presence of residual Na⁺ environments that are still nearby Mn³⁺ ions.}

3.5. XANES. To investigate the change of Mn oxidation state and local structure during cycling, *ex situ* X-ray absorption near edge structure (XANES) analyses were performed on the

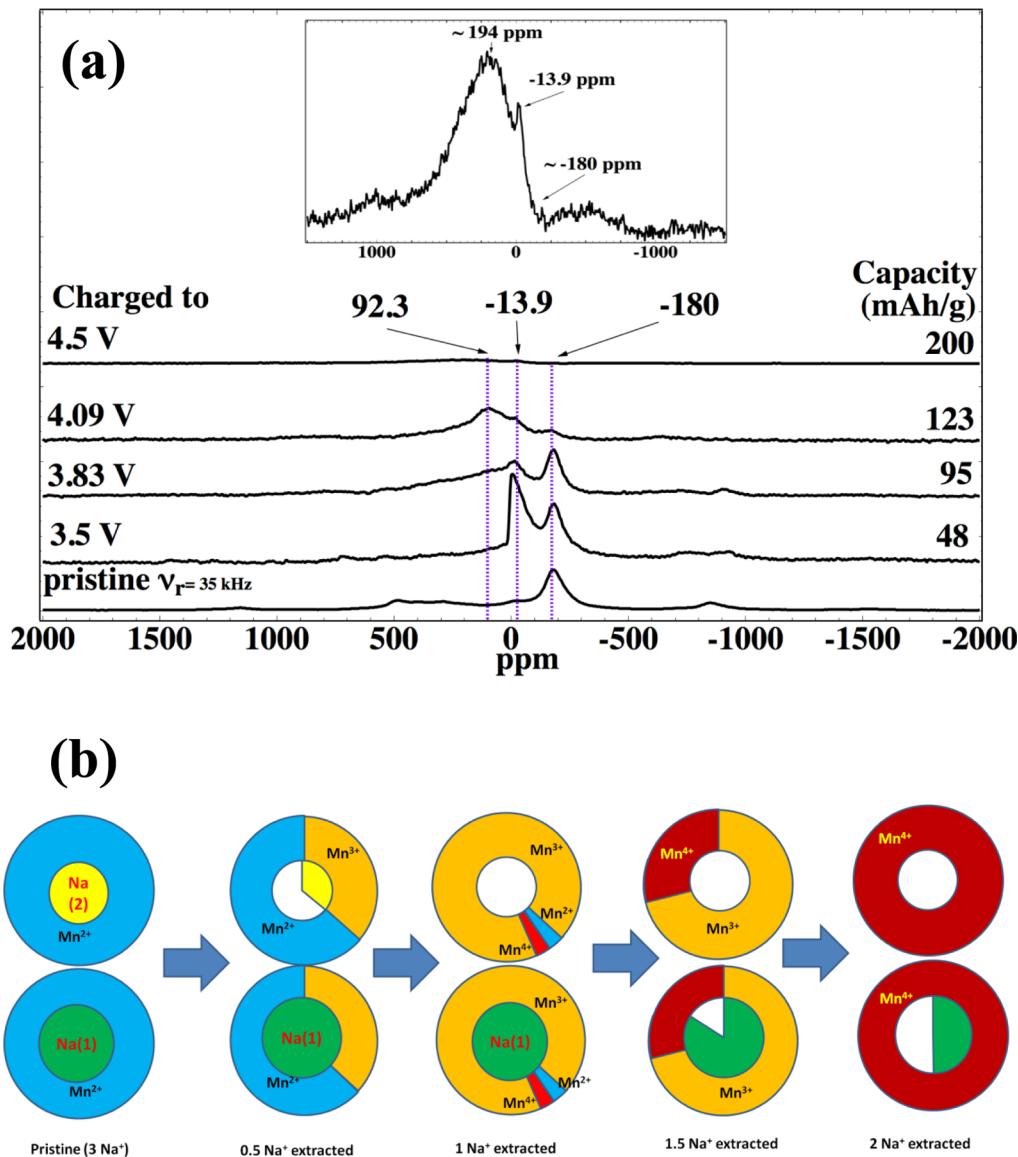


Figure 8. (a) ^{23}Na MAS NMR spectra of sidorenkite at different stages of charge. Spectra were acquired on a 4.7 T magnet at spinning speeds of 35–38 kHz. Inset is an enlargement of the ^{23}Na MAS NMR spectrum of material charged to 4.5 V. (b) Schematic illustration of the extraction sequence of Na ions from Na(2) and Na(1) sites and corresponding oxidation states of Mn in the first cation coordination shell surrounding the Na ions. Green, Na(1); yellow, Na(2); white, empty site; blue, Mn^{2+} ; yellow, Mn^{3+} ; red, Mn^{4+} . The schematic does not illustrate the physical distribution of species within a particle but only the relative ratio of the ions in the samples at different stages.

pristine, charged, and discharged sidorenkite samples (Figure 10). Upon charging, the main edge shifts toward higher energy, accompanied by the lowering of the edge crest and the increase of a shoulder at ~ 6565 eV (Figure 10a). At a charging voltage higher than 4.3 V, the main edge crest shifts to higher energy (~ 6560 eV) and starts to increase in intensity with increasing voltage. The shift of edge position is consistent with the increase of oxidation state upon charging. During discharge, the opposite occurs (Figure 10b). The sample discharged to 2.0 V shows a spectrum very similar to pristine sidorenkite (Figure 10b, black and brown lines), except for a slightly diminished height of the peak crest and higher shoulder at ~ 6565 eV, suggesting the reaction is highly reversible. A zoom of the spectra around the pre-edge is shown in Figure S9. The shift of the pre-edge peaks shows a trend that is similar to that of the main edge. However, due to the very different bonding environment of the carbonophosphates, accurate oxidation

states cannot be readily extracted by comparison with oxide standards (MnO , Mn_2O_3 , and MnO_2 , etc.;⁵¹ see Figure S8 in the Supporting Information for more details). A similar difficulty was also reported for LiMnPO_4 and Li–Mn–O–N compounds.^{51,53} In sidorenkite, the MnO_6 octahedrons share corners with PO_4 tetrahedrons and share edges with CO_3 groups, resulting in a bonding environment that is quite different from that found in an oxide (and consistent with the different potential for Mn^{2+} oxidation). This results in noticeable shifts of the edge positions.

4. DISCUSSION

4.1. Electrochemical Performances. We have investigated the electrochemical properties and structural changes upon desodiation of sidorenkite ($\text{Na}_3\text{MnPO}_4\text{CO}_3$) by *in situ* and *ex situ* analytical techniques. Our results show that this carbonophosphate compound is a promising intercalation

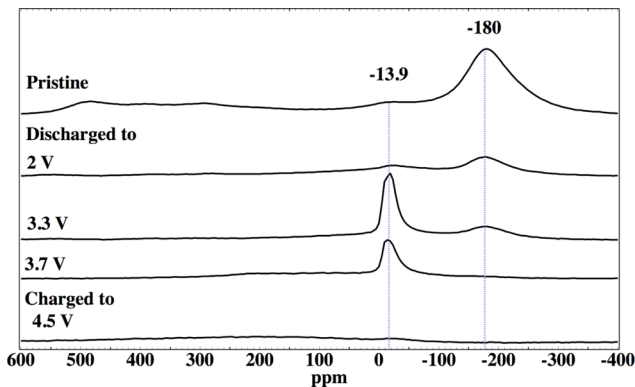


Figure 9. ²³Na MAS NMR spectra of pristine sidorenkite, sidorenkite charged to 4.5 V and then discharged to different potentials. All spectra were acquired on a 4.7 T magnet at a spinning speed of 38 kHz, except for that of the pristine material, which was acquired at a spinning speed of 35 kHz.

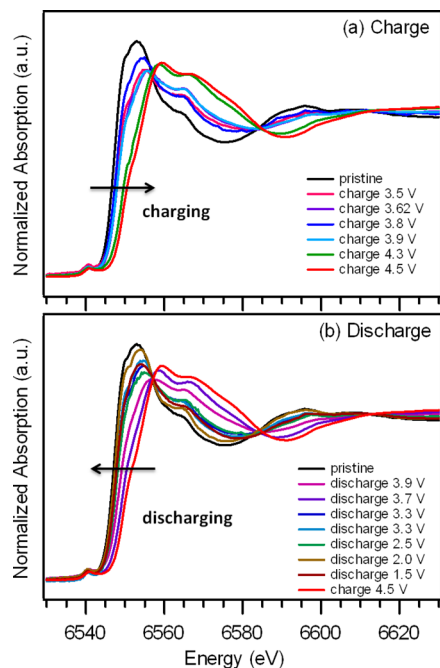


Figure 10. *Ex situ* XANES spectra of sidorenkite samples (a) charged and (b) discharged at different voltages.

cathode material for NIBs. The theoretical capacity of sidorenkite (191 mAh/g) is higher than most of the known polyanion cathode materials, such as NaFePO₄ (154 mAh/g) and NaFeSO₄F (138 mAh/g). While the theoretical capacity of O₃ structured layered oxides is higher, most of them can only cycle less than 50% of their theoretical capacities. A higher fraction (~72%) of the theoretical capacity is achieved by Komaba et al.³ for P2 structured Na_{0.67}Fe_{0.5}Mn_{0.5}O₂, however, with a low average voltage (2.75 V). For sidorenkite, about 66% of the theoretical capacity can be obtained so far, which is superior to most oxide materials. Further optimization of the synthesis conditions, particle size, morphology, and improvement on the electronic conductivity may lead to even higher capacity. The equilibrium intercalation voltage of sidorenkite (~3.7 V), taken as the average between the anodic and cathodic peaks in Figure 4b, is higher than that of most of the oxide cathode materials.^{1,3} This higher voltage of the Mn redox

couples is due to the inductive effect provided by the polyanionic groups (compare, for example, the voltage for Na_xMnO₂⁸ (~2.5 V) with the Mn³⁺/Mn⁴⁺ voltage observed in the sidorenkite). The inductive effect (i.e., the increase in voltage from the oxide voltage) is however only moderate due to the close proximity of the carbon atom in the carbonate ion and the Mn ion. Consistent with this, we previously observed that the Li-based sidorenkite structure offers an unusually low voltage for the Mn²⁺/Mn³⁺ couple as compared to the average phosphate cathode.^{20,21} In a LiMnPO₄ olivine phosphate structure, each Mn–O octahedron shares corners with six PO₄ tetrahedra, while in the sidorenkite structure, each Mn–O octahedron shares corners with four PO₄ tetrahedra and shares an edge with the triangle of the CO₃²⁻ anion. This lower voltage is beneficial as it offers the possibility for two-electron activity within the voltage window of stability of the electrolyte. This advantage for Li-based sidorenkite cathodes extends to Na technology. As a result of both high voltage and reasonable capacity, the specific energy of sidorenkite obtained from integrating the voltage profile in the first discharge is 374 Wh/kg. The theoretically calculated specific energy, using the *ab initio* calculated voltages is 678 Wh/kg.

Several factors may cause the lower than theoretical discharge capacity: (1) We have no information on the electronic or ionic conductivity of this material, and transport limitations could cause high polarization toward the end of charge or discharge, thereby limiting the charge and/or discharge capacity that can be achieved. (2) The sample is heavily ball milled, and it is likely that this causes defects in the material. (3) The charging voltage that can be applied is limited due to the anodic stability limit of the electrolyte. While electrolytes used in LIBs have been extensively studied for over 20 years and are optimized for this application, NIB electrolytes are much less studied, and there is currently no available commercial NIB electrolyte. It is possible that the electrolyte used here has non-negligible effects on the capacity and cyclability of the cathode materials. (4) Some reactivity of the material with air is likely because the Na extraction voltage at the beginning of charge is below 3 V (in the second cycle). While care was taken to prevent air exposure of our samples, some reaction cannot be excluded, particularly during electrode construction. The fact that the second charge curve has slightly more charge capacity at low potential than the first charge may be indicative of the fact that the sample lost a small amount of Na to air exposure before electrochemical testing, supporting this suggestion. (5) The high charge voltage may possibly cause the material to partly decompose on the surface and/or may lead to the release of CO₂. But currently, we do not have experimental observations to prove or disprove this.

The discharge capacity of sidorenkite drops noticeably in the first few cycles and then stabilizes at ~100 mAh/g in the following cycles, indicating that the framework consisting of MnO₆ octahedra and PO₄ groups is fairly stable upon Na insertion/extraction. Both NMR and XANES spectra confirmed that the sample discharged to 2 V has a local structure that is similar to the pristine material. A solid solution pathway of sidorenkite during electrochemical cycling has been suggested by *in situ* XRD measurement. Such a solid solution pathway has been proposed to be a possible reason for the fast Li⁺ diffusion in LiFePO₄ material due to the lower excitation energy required as compared to a high-energy penalty nucleation process.⁵⁵ However, in this preliminary test the rate performance of sidorenkite is poor. It is not clear yet what the rate limiting

factors are, e.g., ionic conductivity, electronic conductivity, or surface passivation.

4.2. Two-Electron Reaction and Na Extraction Sequence.

Sidorenkite has a complex structure containing both PO_4 and CO_3 groups and has not been widely studied. Due to the difficulty in finding standard compounds with comparable structure, the oxidation state of Mn at different states of charge/discharge cannot be readily extracted from *ex situ* XANES spectra. However, based on a number of indirect results, we believe that the $\text{Mn}^{3+}/\text{Mn}^{4+}$ redox couple is active in sidorenkite. In the first cycle, the electrochemically measured charge capacity corresponds to the extraction of slightly more than two Na ions per formula unit. While some of this capacity is likely to be from electrolyte breakdown, even the discharge capacity of 125 mAh/g corresponds to 1.3 Na^+ insertion per formula unit. Both results imply that $\text{Mn}^{2+}/\text{Mn}^{3+}$ and $\text{Mn}^{3+}/\text{Mn}^{4+}$ redox couples are active. Furthermore, the voltages of the two plateaus are consistent with the computationally predicted intercalation voltage for $\text{Mn}^{2+}/\text{Mn}^{3+}$ and $\text{Mn}^{3+}/\text{Mn}^{4+}$, which are around 3.1 and 4.0 V, respectively. Additionally, ^{23}Na NMR spectroscopy provides further evidence for a two-electron reaction: at the top of charge, the Na(2) and Na(1) sites are completely and partly emptied, respectively. This also indicates more than one Na per formula unit is removed, which must result in the formation of some Mn^{4+} to compensate the charge.

In a closer examination of the NMR spectra, the population of the Na(2) site decreases on charging to 3.5 V (Figure 8), and the Na(2) sites are completely removed at ~ 3.8 V. This is in agreement with the voltages computed for extracting Na from the Na(2) and Na(1) site paired with $\text{Mn}^{2+}/\text{Mn}^{3+}$ oxidation, the computed results of 3.11 V (Na(2)) and 3.24 V (Na(1)) indicating that Na should be first extracted from the Na(2) site. The NMR signal arising from the Na(1) ions, which are not extracted until the second process, is sensitive to the oxidation of Mn^{2+} to Mn^{3+} , and the broad asymmetric resonance observed at -13 ppm is ascribed to Na(1) ions nearby both Mn^{2+} and Mn^{3+} . This behavior supports a solid solution mechanism for the first process, since a two phase reaction mechanism would result in Na(1) ions nearby either Mn^{2+} or Mn^{3+} ions only. The extraction of Na^+ ions above 3.8 V occurs from the Na(1) site as indicated by the decrease in the Na(1) site peak area compared to the pristine material and a further shift in the ^{23}Na resonances toward higher frequencies (Figure 8). Figure 8b schematically shows the extraction sequence of Na from different sites and the corresponding change of the Mn oxidation state. The desodiation process can be summarized as (1) the extraction of Na^+ from the Na(2) site, with the local environment of Na(1) changing from pure Mn^{2+} to a mixed $\text{Mn}^{2+}/\text{Mn}^{3+}$ environment and (2) extraction of Na^+ at the Na(1) site.

Electrochemical intercalation of Na^+ is not completely reversible, and only 1.3 Na^+ ions per formula unit are reintercalated into the structure. The sequences of electrochemical intercalation of Na^+ ions in the sidorenkite structure do not completely mirror those seen for electrochemical extraction, which may account for the slight asymmetry of the charge and discharge curves. For example, the resonance at ~ 92 ppm, due to a mixed $\text{Mn}^{3+}/\text{Mn}^{4+}$ environment, is not observed at 3.7 V during discharge (Figure S4). Instead, a resonance at approximately -13 ppm dominates the ^{23}Na MAS NMR spectra of the materials discharged to 3.7 and 3.3 V, which is indicative of the presence of Mn^{2+} and Mn^{3+} ions. The

observation of this resonance at 3.7 V is somewhat surprising because this voltage should correspond to the end of the $\text{Mn}^{4+}/\text{Mn}^{3+}$ process but most likely reflects an overlap between the potentials associated with the two (solid-solution) processes and the different kinetics of the two processes. Reinsertion of the Na(2) ions is seen at 3.3 V. The total intensity of the Na(1) sites in the electrode material discharged to 2 V is only 62% of the area of the Na(1) site in pristine material, indicating that only 0.24 Na^+ ions per formula unit were intercalated in the Na(1) site. Thus the capacity loss appears to be due to the difficulty of reinserting Na into the structure. Since both the Na(1) environments due to Na nearby $\text{Mn}^{3+}/\text{Mn}^{2+}$ and Mn^{2+} only are observed, along with a broader component at higher frequencies (due to $\text{Mn}^{3+}/\text{Mn}^{4+}$; Figure S6), capacity loss appears to occur for both processes.

Activating both the $\text{Mn}^{2+}/\text{Mn}^{3+}$ and $\text{Mn}^{3+}/\text{Mn}^{4+}$ redox couples is rare in intercalation materials. In most phosphates, obtaining even reasonable capacity from a single Mn redox couple has proven to be difficult, as demonstrated by the poor performance of LiMnPO_4 . The voltage of the $\text{Mn}^{3+}/\text{Mn}^{4+}$ redox couple is generally predicted to be high and is difficult to activate in Li-intercalation materials with current electrolytes, though a clever experiment on doped olivines has recently shown $\text{Mn}^{3+}/\text{Mn}^{4+}$ activity in a Li-intercalation system.⁵⁶ On the other hand, in the pyrophosphates, the stronger inductive effect pushes the $\text{Mn}^{3+}/\text{Mn}^{4+}$ to very high voltage, completely inhibiting any two-electron process.⁵⁷ Overall, the electrochemical activation of both Mn couples is very rare for polyanion materials. Hence, our demonstration of a two-electron intercalation in sidorenkite by means of electrochemical and NMR experiments creates hope that high capacity, high voltage Na-intercalation cathodes can be designed based on the safe and inexpensive Mn element.

5. CONCLUSIONS

In this work, we have reported the synthesis, electrochemical tests, and structural characterization of a new intercalation cathode material for NIBs. Our preliminary results show that sidorenkite has a high average voltage (3.7 V), high capacity (~ 125 mAh/g), and good cyclability. In addition to the previously reported Li compound,²¹ this material provides a second example that shows that carbonophosphates are a new class of polyanion compounds that can allow for reversible intercalation reactions of alkaline metals. More importantly, both the $\text{Mn}^{2+}/\text{Mn}^{3+}$ and $\text{Mn}^{3+}/\text{Mn}^{4+}$ can be activated in sidorenkite, giving rise to the high capacity and energy density. The synthesis of sidorenkite is relatively simple, low cost, and facile to scale up. As we reported earlier,⁵⁸ many metals other than Mn can also adopt the sidorenkite structure, and the encouraging electrochemical performance reported here from the Mn form suggests that there are other promising intercalation compounds in this carbonophosphate chemical class for both Na- and Li-ion batteries.

■ ASSOCIATED CONTENT

Supporting Information

Rietveld refinement results of sidorenkite. In situ XRD patterns and setup, summary of the shifts observed in sidorenkite ^{23}Na NMR spectra, projection MATPASS method, ^{23}Na NMR spectra, and Mn XANES valence-edge position calibration curve (PDF). Crystallographic file (CIF). This material is available free of charge via the Internet at <http://pubs.acs.org>.

AUTHOR INFORMATION

Corresponding Author

*E-mail: gceder@MIT.EDU.

Notes

The authors declare no competing financial interest.

ACKNOWLEDGMENTS

H.C., Q.H., G.H., and G.C. acknowledge funding support for the synthesis of sidorenkite from the U.S. Department of Energy BATT program under contract no. DE-AC02-05CH11231. Y.T. acknowledges funding support from C. M. Hansel. O.Z. and C.P.G. thank the Office of FreedomCAR and Vehicle Technologies of the U.S. Department of Energy under Contract No. DE-AC03-76SF00098, via subcontract No. 680711 with the Lawrence Berkeley National Laboratory, for support. H.C. thanks Dr. Peter Stephens, Dr. Jianming Bai, Dr. Xiqian Yu, and Nancy Twu for their help with synchrotron X-ray diffraction and absorption data collection.

REFERENCES

- (1) Ellis, B. L.; Nazar, L. F. *Curr. Opin. Solid State Mater. Sci.* **2012**, *16*, 168.
- (2) Ong, S. P.; Chevrier, V. L.; Hautier, G.; Jain, A.; Moore, C.; Kim, S.; Ma, X. H.; Ceder, G. *Energy Environ. Sci.* **2011**, *4*, 3680.
- (3) Yabuuchi, N.; Kajiyama, M.; Iwatate, J.; Nishikawa, H.; Hitomi, S.; Okuyama, R.; Usui, R.; Yamada, Y.; Komaba, S. *Nat. Mater.* **2012**, *11*, 512.
- (4) Abouimrane, A.; Weng, W.; Eltayeb, H.; Cui, Y. J.; Niklas, J.; Poluektov, O.; Amine, K. *Energy Environ. Sci.* **2012**, *5*, 9632.
- (5) Yamamoto, T.; Nohira, T.; Hagiwara, R.; Fukunaga, A.; Sakai, S.; Nitta, K.; Inazawa, S. *J. Power Sources* **2012**, *217*, 479.
- (6) Berthelot, R.; Carlier, D.; Delmas, C. *Nat. Mater.* **2011**, *10*, 74.
- (7) Sauvage, F.; Laffont, L.; Tarascon, J. M.; Baudrin, E. *Inorg. Chem.* **2007**, *46*, 3289.
- (8) Ma, X. H.; Chen, H. L.; Ceder, G. *J. Electrochem. Soc.* **2011**, *158*, A1307.
- (9) Komaba, S.; Yabuuchi, N.; Nakayama, T.; Ogata, A.; Ishikawa, T.; Nakai, I. *Inorg. Chem.* **2012**, *51*, 6211.
- (10) Kim, D.; Lee, E.; Slater, M.; Lu, W. Q.; Rood, S.; Johnson, C. S. *Electrochem. Commun.* **2012**, *18*, 66.
- (11) Kim, D.; Kang, S. H.; Slater, M.; Rood, S.; Vaughney, J. T.; Karan, N.; Balasubramanian, M.; Johnson, C. S. *Adv. Energy Mater.* **2011**, *1*, 333.
- (12) Trad, K.; Carlier, D.; Croguennec, L.; Wattiaux, A.; Lajmi, B.; Ben Amara, M.; Delmas, C. *J. Phys. Chem. C* **2010**, *114*, 10034.
- (13) Trad, K.; Carlier, D.; Croguennec, L.; Wattiaux, A.; Ben Amara, M.; Delmas, C. *Chem. Mater.* **2010**, *22*, 5554.
- (14) Lee, K. T.; Ramesh, T. N.; Nan, F.; Botton, G.; Nazar, L. F. *Chem. Mater.* **2011**, *23*, 3593.
- (15) Oh, S. M.; Myung, S. T.; Hassoun, J.; Scrosati, B.; Sun, Y. K. *Electrochem. Commun.* **2012**, *22*, 149.
- (16) Zaghib, K.; Trottier, J.; Hovington, P.; Brochu, F.; Guerfi, A.; Mauger, A.; Julien, C. M. *J. Power Sources* **2011**, *196*, 9612.
- (17) Barpanda, P.; Chotard, J. N.; Recham, N.; Delacourt, C.; Ati, M.; Dupont, L.; Armand, M.; Tarascon, J. M. *Inorg. Chem.* **2010**, *49*, 7401.
- (18) Khomyakov, A. *Int. Geol. Rev.* **1980**, *22*, 811.
- (19) Kurova, T. A.; Shumyatskaya, N. G.; Vornkov, A. A.; Pyatenko, Y. A. *Mineral. Zh.* (1979-2002) **1980**, *2*, 65.
- (20) Hautier, G.; Jain, A.; Chen, H. L.; Moore, C.; Ong, S. P.; Ceder, G. *J. Mater. Chem.* **2011**, *21*, 17147.
- (21) Chen, H. L.; Hautier, G.; Jain, A.; Moore, C.; Kang, B.; Doe, R.; Wu, L. J.; Zhu, Y. M.; Tang, Y. Z.; Ceder, G. *Chem. Mater.* **2012**, *24*, 2009.
- (22) Zeng, D.; Cabana, J.; Bréger, J.; Yoon, W.-S.; Grey, C. P. *Chem. Mater.* **2007**, *19*, 6277.
- (23) Kim, J.-S.; Johnson, C. S.; Vaughney, J. T.; Thackeray, M. M.; Hackney, S. A.; Yoon, W.; Grey, C. P. *Chem. Mater.* **2004**, *16*, 1996.
- (24) Jiang, M.; Key, B.; Meng, Y. S.; Grey, C. P. *Chem. Mater.* **2009**, *21*, 2733.
- (25) Grey, C. P.; Dupré, N. *Chem. Rev.* **2004**, *104*, 4493.
- (26) Qian, D. N.; Hinuma, Y.; Chen, H. L.; Du, L. S.; Carroll, K. J.; Ceder, G.; Grey, C. P.; Meng, Y. S. *J. Am. Chem. Soc.* **2012**, *134*, 6096.
- (27) Chen, H. L.; Grey, C. P. *Adv. Mater.* **2008**, *20*, 2206.
- (28) Ellaboudy, A.; Tinkham, M. L.; Van Eck, B.; Dye, J. L.; Smith, P. B. *J. Phys. Chem.* **1984**, *88*, 3852.
- (29) Hanna, J. V.; Smith, M. E.; Whitfield, H. J. *J. Am. Chem. Soc.* **1996**, *118*, 5772.
- (30) Kim, J.; Dye, J. L. *J. Phys. Chem.* **1990**, *94*, 5399.
- (31) Koller, H.; Engelhardt, G.; Kentgens, A. P. M.; Sauer, J. *J. Phys. Chem.* **1994**, *98*, 1544.
- (32) Wong, A.; Wu, G. *J. Phys. Chem. A* **2000**, *104*, 11844.
- (33) Xu, M.; Harris, K. D. M. *Cryst. Growth Des.* **2008**, *8*, 6.
- (34) Carlier, D.; Blangero, M.; Ménétrier, M.; Pollet, M. l.; Doumerc, J.-P.; Delmas, C. *Inorg. Chem.* **2009**, *48*, 7018.
- (35) Carlier, D.; Cheng, J. H.; Berthelot, R.; Guignard, M.; Yoncheva, M.; Stoyanova, R.; Hwang, B. J.; Delmas, C. *Dalton Trans.* **2011**, *40*, 9306.
- (36) Beek, J. D. v. *J. Magn. Reson.* **2007**, *187*, 19.
- (37) Zorin, V. *GSim*, 0.20.1 ed; 2011. <http://sourceforge.net/projects/gsim>. p NMR viewing/processing toolNMR viewing/processing tool.
- (38) Rehr, J. J.; Deleon, J. M.; Zabinsky, S. I.; Albers, R. C. *J. Am. Chem. Soc.* **1991**, *113*, 5135.
- (39) Kresse, G.; Furthmüller, J. *Comput. Mater. Sci.* **1996**, *6*, 15.
- (40) Perdew, J.; Burke, K.; Ernzerhof, M. *Phys. Rev. Lett.* **1996**, *77*, 3865.
- (41) Blöchl, P. *Phys. Rev. B* **1994**, *50*, 17953.
- (42) Dudarev, S. L.; Savrasov, S. Y.; Humphreys, C. J.; Sutton, A. P. *Phys. Rev. B* **1998**, *57*, 1505.
- (43) Wang, L.; Maxisch, T.; Ceder, G. *Phys. Rev. B* **2006**, *73*, 195107.
- (44) Jain, A.; Hautier, G.; Moore, C. J.; Ong, S. P.; Fischer, C. C.; Mueller, T.; Persson, K. A.; Ceder, G. *Comput. Mater. Sci.* **2011**, *50*, 2295.
- (45) Aydinol, M.; Kohan, A.; Ceder, G.; Cho, K.; Joannopoulos, J. *Phys. Rev. B* **1997**, *56*, 1354.
- (46) Hart, G. L. W.; Forcade, R. W. *Phys. Rev. B* **2008**, *77*, 224115.
- (47) Chevrier, V. L.; Ong, S. P.; Armiento, R.; Chan, M. K. Y.; Ceder, G. *Phys. Rev. B* **2010**, *82*, No. 235121.
- (48) Zhou, F.; Cococcioni, M.; Kang, K.; Ceder, G. *Electrochem. Commun.* **2004**, *6*, 1144.
- (49) Massiot, D.; Bessada, C.; Coutures, J. P.; Taulelle, F. *J. Magn. Reson.* **1990**, *90*, 231.
- (50) Kim, J.; Middlemiss, D. S.; Chernova, N. A.; Zhu, B. Y. X.; Masquelier, C.; Grey, C. P. *J. Am. Chem. Soc.* **2010**, *132*, 16825.
- (51) Cabana, J.; Dupré, N.; Gillot, F.; Chadwick, A. V.; Grey, C. P.; Palacin, M. R. *Inorg. Chem.* **2009**, *48*, 5141.
- (52) Grey, C. P.; Lee, Y. J. *Solid State Sci.* **2003**, *5*, 883.
- (53) Nedoseykina, T.; Kim, M. G.; Park, S. A.; Kim, H. S.; Kim, S. B.; Cho, J.; Lee, Y. *Electrochim. Acta* **2010**, *55*, 8876.
- (54) Wilcke, S. L.; Lee, Y. J.; Cairns, E. J.; Reimer, J. A. *Appl. Magn. Reson.* **2007**, *32*, 547.
- (55) Malik, R.; Zhou, F.; Ceder, G. *Nat. Mater.* **2011**, *10*, 587.
- (56) Memm, M.; Axmann, P.; Wohlfahrt-Mehrens, M. Abstract #321; The 15th International Meeting on Lithium Batteries; Montreal, Canada, June 27 to July 3, 2010.
- (57) Zhou, H.; Upadhyay, S.; Chernova, N. A.; Hautier, G.; Ceder, G.; Whittingham, M. S. *Chem. Mater.* **2011**, *23*, 293.
- (58) Chen, H. L.; Hautier, G.; Ceder, G. *J. Am. Chem. Soc.* **2012**, *134*, 19619.